

# Observation of High Energy Neutrinos from the Daya Bay Nuclear Power Plant

Neill D. Raper, Jim Napolitano, and Don Jones

August 10, 2016

## Abstract

We observe a nonzero flux of neutrinos with energies greater than 8 MeV using the “Near Hall” detectors of the Daya Bay Reactor Neutrino Experiment. In this region, the signal-to-background ratio is significantly less than unity. Our technique is to correlate the rate of inverse beta decay (IBD) candidates as a function of (effective) reactor power  $W_{\text{eff}}$ . On a scale where  $W_{\text{eff}} = 1$  means all reactors at full power, we collect IBD rates with  $0.5 \leq W_{\text{eff}} \leq 1$  as reactor cores are removed and replaced for refueling. The extrapolated background rate (for  $W_{\text{eff}} = 0$ ) agrees with independent estimates, and the reactor-associated signal can be extracted from the slope. The signal for  $E_{\bar{\nu}_e} \leq 8$  MeV agrees with our published result from integrating over all runs and as a function of energy. The signal for  $E_{\bar{\nu}_e} \geq 8$  MeV appears to be nonzero, and can only come from a handful of fission isotopes. There are important implications for models of calculating the neutrino flux, as well as for backgrounds from nuclear power plants for “relic supernova neutrino” experiments.

## 1 Motivation and Challenge

Nuclear power plant reactors are popular sources of  $\bar{\nu}_e$  for fundamental physics experiments that have yielded important new results [1, 2, 3, 4, 5, 6, 7, 8, 9, 10, 11]. These results are possible, despite the fact that the intensity and energy spectrum of  $\bar{\nu}_e$  from nuclear power plants are notoriously difficult to calculate [12, 13, 14, 15, 16, 17, 18, 19], by making measurements both “near” and “far from” the reactor cores. Nevertheless, knowledge of the reactor spectrum remains a significant component of the limiting systematic error [7]. Furthermore, high statistics neutrino flux measurements from power plants, for example Daya Bay [20], indicate a peculiar and unforeseen “shoulder” in the neighborhood of 5 MeV. The origin of this shoulder remains unsolved, but it may have to do with different fissile components in a typical nuclear generating station, and their evolution over time [21].

The neutrino spectrum contains literally thousands of components, from the very many different nuclear beta decays of fission fragments in the reactor core. Nearly all of these

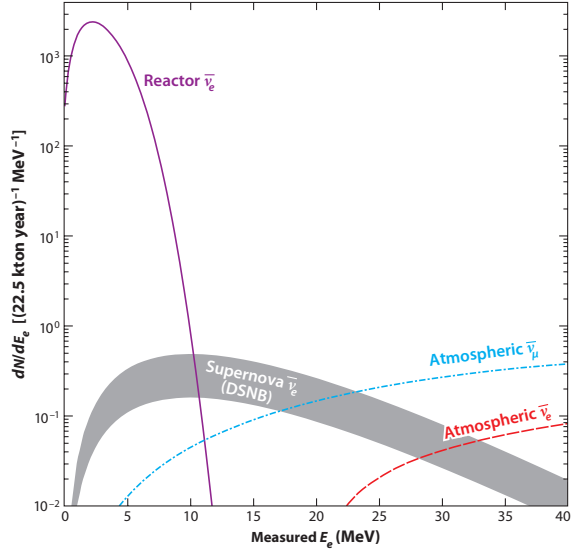


Figure 1: The Diffuse Supernova Neutrino Background (DSNB) spectrum and expected signals from other sources, as a function of energy, from [22]. The accessible signal region is bounded from above by atmospheric neutrinos, and from below by neutrinos from nuclear power plants. It is clear that the shape of the latter at high energies needs to be understood clearly.

decays, however, have relatively low  $Q$ -values. That is, the endpoint energies of the beta decays are predominantly less than several MeV. This means that a measurement of the highest neutrino energies can point to relatively few specific isotopes, and this can inform details of the database one might use to construct the spectrum.

There is another motivation for studying the nuclear power plant neutrino spectrum at high energies. A “relic” neutrino background permeates all space, called the Diffuse Supernova Neutrino Background [22]. Measuring the flux of these neutrinos is useful for understanding supernovae and their role in the evolution of the universe. It may be possible to measure this flux using large underground detectors [23], but the accessible signal lies in a narrow energy region, bounded by atmospheric neutrino production above and nuclear power plant neutrinos below. See Fig. 1. Clearly we need to understand the high energy tail of the nuclear power plant neutrino spectrum, in order to reliably extract the DSNB signal.

The main challenge to measuring the high energy neutrino spectrum is that the IBD spectrum falls rapidly above several MeV, and at some point is underneath cosmogenic or other backgrounds. These backgrounds are not known precisely enough to reliably subtract them from the total in order to extract the signal.

Figure 2 illustrates this difficulty. The figure shows typical prompt energy spectra from Daya Bay, at the near and far detector sites. The background levels shown are estimated in various ways, and are a small contribution for most of the energy spectrum. Neglecting neutron recoil kinetic energy, the prompt energy (which includes the annihilation photons when the final state positron encounters an atomic electron) is

$$E \equiv E_{\text{prompt}} = E_{\bar{\nu}_e} - (m_n - m_p)c^2 - m_e c^2 + 2m_e c^2 = E_{\bar{\nu}_e} - 0.782 \text{ MeV} \quad (1)$$

Extracting the neutrino energy spectrum above  $\approx 8$  MeV ( $E_{\text{prompt}}$  greater than  $\approx 7$  MeV) will have to rely on a technique that does not simply estimate the background level.

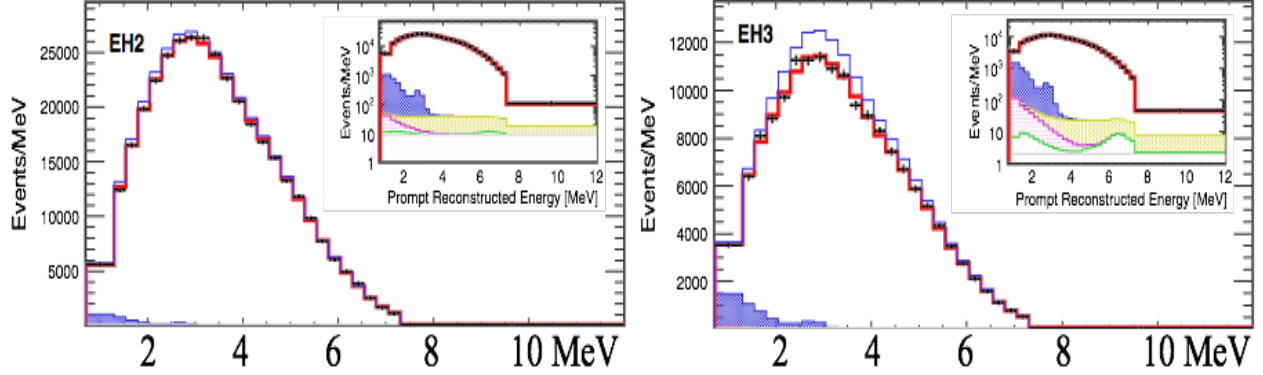


Figure 2: Prompt energy spectra from near and far detectors at Daya Bay, from [6].

## 2 Effective Reactor Power and Fluctuations

Our approach is to make use of the regular fluctuations in the individual Daya Bay and Ling Ao power station outputs, to linearly extrapolate to zero power. The slope of this line gives us the reactor-correlated neutrino rate, and the intercept yields the background rate. That is, the intercept gives a result that should be consistent with other background determinations, and the slope will yield an independent measurement of the reactor flux at low energies, and give us the ability to extend the flux measurement to high energies.

The power station outputs fluctuate because they have two (Daya Bay) or four (Ling Ao) cores which are refueled regularly. The cores are in pairs, and no more than one of each pair is refueled at the same time. Therefore, the EH1 near detectors see a cluster of runs with the power at half maximum, and a cluster near full power, with some scattering in between. The EH2 detectors see a more evenly distributed set of reactor powers between half and full. Of course, this pattern is diluted to some extent, because of the Ling Ao flux at EH1, and the Daya Bay flux at EH2.

The six reactors of the power plant are effectively identical, each with a maximum thermal power of 2.9 GW [20]. We define a (dimensionless) “Effective Reactor Power”  $W_{\text{eff}}$  as the total power seen by the sum of the six reactor cores, weighted by their inverse square distance to the detectors, and also neutrino disappearance probability, scaled to the maximum power output. That is,

$$W_{\text{eff}}(t) = \frac{\sum_{i=1}^6 (W_i^{\text{th}}/L_i^2) P_{\text{sur}}(\bar{E}_\nu, L_i)}{2.9 \text{ GW} \times \sum_{i=1}^6 (1/L_i^2)} \quad (2)$$

where  $W_i^{\text{th}}(t)$  is the thermal power of reactor  $i$  as a function of time, and  $L_i$  is the distance of each reactor core to the experimental hall. The neutrino survival probability  $P_{\text{sur}}(E_\nu, L_i)$  is given by the simple two-neutrino oscillation formula

$$P_{\text{sur}}(E_\nu, L_i) = 1 - \sin^2 2\theta \sin^2 \left( 1.27 \Delta m^2 \frac{L_i}{E_\nu} \right) \quad (3)$$

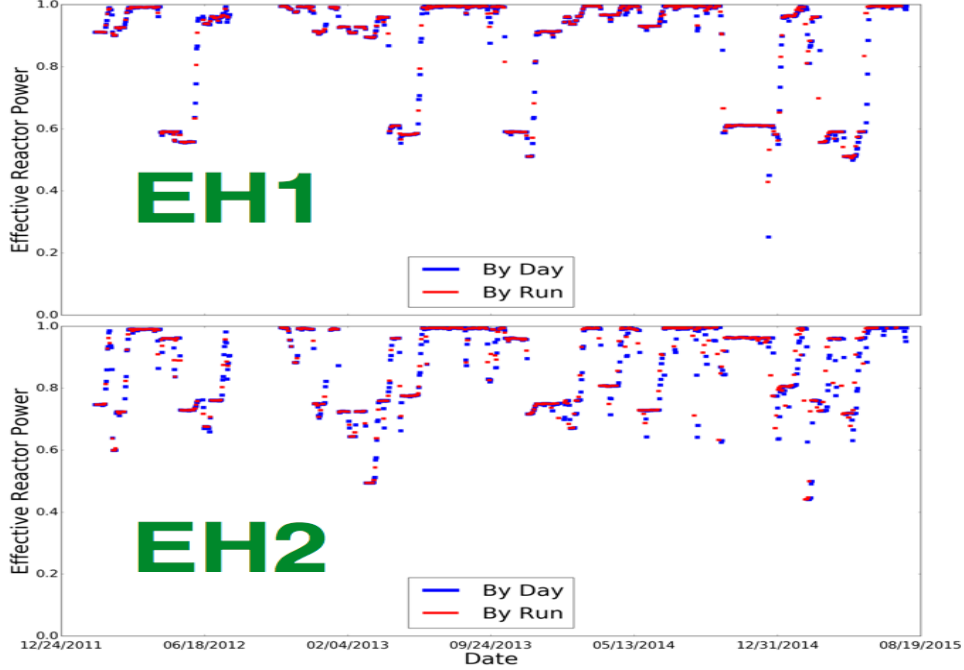


Figure 3: Effective (dimensionless) reactor power in EH1 and EH2 from the distribution in space and time of the reactor cores at the Daya Bay Nuclear Power Plant complex. Two cores are located close to EH1, and four cores are near EH2. Refueling is carried out on one core of a pair at any given time.

where  $\sin^2 2\theta = 0.084 \pm 0.005$  and  $\Delta m^2 = (2.42 \pm 0.11) \times 10^{-3} \text{ eV}^2$  are taken from [7], and  $E_\nu = E + 0.782 \text{ MeV}$  gives the energy of the neutrino. This is a small effect, especially for the near halls, but has noticeable consequences later when it is used for the extrapolation to zero power.

Figure 3 plots  $W_{\text{eff}}$  as a function of time, for each of the two near halls. The blue points are calculated from Eq. 2, based on daily reactor power data, with neutrino survival probability set to unity. The pattern of fluctuations between half and full power are clear, with EH1 showing clustering mainly around  $W_{\text{eff}} = 0.5$  and one.

Figure 3 also illustrates the results of an interpolation procedure to determine the effective reactor power integrated over runs. We have access to the individual reactor core powers only on a daily basis, but we analyze the data grouped into runs. A run, on the other hand, typically lasts about 1.5 days. A simple linear interpolation is used, based on the amount of time that a run spends in one calendar day versus the next. The red points in Fig. 3 show the result of the linear interpolation.

The next step is to take this effective reactor power, integrated over each run, and correlate it against the number of IBD candidates in that run. This linear correlation will give us a slope, from which we can determine the reactor neutrino yield, and an intercept which we can cross check against independent estimates of backgrounds.

### 3 Determining the Yield

The prompt energy spectrum of detected  $\bar{\nu}_e$ , which we call the “yield”  $Y(E)$  with appropriate normalization, is essentially the product of the differential neutrino energy spectrum  $S(E_\nu)$  and the IBD cross section  $\sigma_{\text{IBD}}(E_\nu)$ . Our job at this step is to experimentally determine  $Y(E)$  by observing a correlation between IBD candidates and effective reactor power.

In order to understand this correlation, it is easiest to write down a formal expression for the number of IBD’s observed in a given time, and then reduce it to a form that shows the dependence on effective reactor power. We will be explicit about the prompt energy bin in which we are working, that is  $E_{\text{lo}} \leq E \leq E_{\text{hi}}$ . We will also be integrating over times that correspond to an individual run.

The number  $\Delta\mathcal{N}$  of IBD events in energy range  $\Delta E = E_{\text{hi}} - E_{\text{lo}}$  over a run time  $\Delta t$ , is

$$\Delta\mathcal{N} = N_p \sum_{i=1}^6 \frac{1}{4\pi L_i^2} \frac{\langle W_i^{\text{th}} \rangle}{\bar{e}_i} \Delta t \int_{E_{\text{lo}}}^{E_{\text{hi}}} P_{\text{sur}}(E_\nu, L_i) \epsilon(E) \sigma_{\text{IBD}}(E_\nu) S_i(E_\nu) dE \quad (4)$$

where  $i$  sums over the six reactor cores,  $N_p$  is the number of protons in the target AD,  $L_i$  is the distance from the AD to reactor core,  $\langle W_i^{\text{th}} \rangle$  is the effective reactor power, averaged over a run, as described in Sec. 2,  $\bar{e}_i$  is the average thermal energy per fission for a reactor core,  $P_{\text{sur}}(E_\nu, L)$  is the oscillation survival probability for a neutrino of energy  $E_\nu$  at a distance  $L$ ,  $\epsilon(E)$  is the detector efficiency for prompt energy  $E$ ,  $\sigma_{\text{IBD}}(E_\nu)$  is the IBD cross section, and  $S_i(E_\nu)$  is the number of  $\bar{\nu}_e$  per fission per unit energy range.

For this analysis, we will assume the same effective fuel mixture for each of the six reactor cores. Therefore  $\bar{e}_i \equiv \bar{e}$  and  $S_i(E_\nu) \equiv S(E_\nu)$  are the same for each reactor. We also will be working in relatively small energy bins, so replace the integral by the integrand at an the appropriate average value of  $E$  or  $E_\nu$ . After some rearranging, Eq. 4 becomes

$$\Delta\mathcal{N} = \frac{N_p}{4\pi} \frac{1}{\bar{e}} \sum_{i=1}^6 \frac{\langle W_i^{\text{th}} \rangle}{L_i^2} P_{\text{sur}}(\bar{E}_\nu, L_i) \epsilon(\bar{E}) \sigma_{\text{IBD}}(\bar{E}_\nu) S(\bar{E}_\nu) \Delta t \Delta E \quad (5)$$

Now use Eq. 2 to write the differential IBD rate as

$$\mathcal{R}(E) \equiv \frac{\Delta\mathcal{N}}{\Delta t \Delta E} = \frac{N_p}{4\pi} \frac{2.9 \text{ GW}}{\bar{e}} \left[ \sum_{i=1}^6 \frac{1}{L_i^2} \right] \langle W_{\text{eff}} \rangle \epsilon(\bar{E}) \sigma_{\text{IBD}}(\bar{E}_\nu) S(\bar{E}_\nu) \quad (6)$$

where  $\langle W_{\text{eff}} \rangle$  is the effective reactor power, averaged over one run, that is, the red points in Fig. 3. Therefore, a plot of  $\mathcal{R}(E)$  versus  $\langle W_{\text{eff}} \rangle$  has a slope that is the product of known factors, the detector efficiency, and  $Y(E) = \sigma_{\text{IBD}}(\bar{E}_\nu) S(\bar{E}_\nu)$ .

Any source of IBD (or IBD-like) events that are not correlated with reactor power, for example from residual accidental coincidences or cosmic ray backgrounds, would contribute an overall constant term added to Eq. 6, but would not affect the slope.

Table 1: Daya Bay data sets used in this analysis.

Data Set	Start	End	Days	Live Time (AD1/2/3 Days)	Live Time (AD4 Days)
P14A	12/24/2011	12/02/2013	710	560	370
P14B	12/02/2013	12/01/2014	364	350	350
P15A	12/24/2011	08/09/2015	1324	1115	925

## 4 Data Selection

The currently available Daya Bay data sets are shown in Table 1. This analysis began with P14A, but the results here are based on P15A.

Runs were only used if they represented more than 0.75 days of live time. Otherwise, standard Daya Bay data selection criteria are used for an inverse beta decay signal using delayed capture on gadolinium [5, 24, 25], but with the upper prompt energy cut increased to 15 MeV. See also [26].

All results in this note use AdSimple for determining the prompt energy from ADC values. The differences with AdScaled, however, are significant [27], and how it affects energies above 8 MeV has yet to be investigated.

## 5 Linear Fitting Procedure

Including a background contribution we rewrite Eq. 6 as

$$\mathcal{R}(E_{\text{lo}}, E_{\text{hi}}) = K \langle W_{\text{eff}} \rangle \epsilon(\bar{E}) Y(\bar{E}_\nu) + \mathcal{R}_0(E_{\text{lo}}, E_{\text{hi}}) \quad (7)$$

where  $K = (2.9 \text{ GW}/\bar{e}) \sum_i (1/L_i^2)$  and  $Y(E_\nu) = \sigma_{\text{IBD}}(E_\nu) S(E_\nu)$ . For any given run, we find the number of IBD candidates in the prompt energy range  $E_{\text{lo}} \leq E \leq E_{\text{hi}}$  to determine the rate  $\mathcal{R}$ , and also determine the effective reactor power  $\langle W_{\text{eff}} \rangle$  time-averaged over the run. Given a collection of runs, we fit a straight line to the data points  $(\langle W_{\text{eff}} \rangle, \mathcal{R})$  to extract the yield  $Y$  and background level  $\mathcal{R}_0$ .

Care must be taken when performing this linear fit. The background rate in the near detectors is on the order of a few events per MeV per day at low energies, and less than one event at high energies. Although the IBD rate is orders of magnitude above this at low energies, it is as small or smaller than the background rate at high energies. Therefore, many, or most, runs will have zero IBD candidates per MeV at high energies. A weighted least squares approach is not valid in this case, and we have to resort to a first principles fit using the method of maximum likelihood.

We follow the procedure outlined in [28], Chapter 38 “Statistics,” especially section 38.2.2 covering “The method of maximum likelihood.” We have binned our data in time over  $N$  runs, so we write the mean number  $\mu$  of events in a run of length  $\Delta T$  and effective power

$\langle W_{\text{eff}} \rangle$  as

$$\mu = \mathcal{R}\Delta T = (A\langle W_{\text{eff}} \rangle + B)\Delta T \quad (8)$$

Our job is to find the constants  $A$  and  $B$  that best represent the collection of runs analyzed. We do this by minimizing the negative log likelihood ratio in Eq.(38.16) from [28], that is

$$-2\mathcal{L}(A, B) = 2 \sum_{i=1}^N \left[ \mu_i(A, B) - n_i + n_i \ln \frac{n_i}{\mu_i(A, B)} \right] \quad (9)$$

where the sum is over runs,  $n_i$  is the observed number of events in a run, and  $\mu_i$  is given by Eq. 8 using  $\langle W_{\text{eff}} \rangle$  for that run. The one standard deviation statistical uncertainties in  $A$  and  $B$  are derived using Eq.(38.16) from [28], that is, by finding the changes in  $A$  or  $B$  which increase the minimum value of  $-2\mathcal{L}$  in Eq. 9 by unity.

The fitting program was checked in two ways. First, a toy Monte Carlo generator was used to create fake data sets with typical mean values  $\mu$  that were less than unity, several, and many, confirming that the program found the generated values in each case. Secondly, for energy bins where the IBD rate is large, a simple linear least squares fit was done for  $A$  and  $B$  and their uncertainties, and these agreed with the values obtained using the likelihood technique.

These linear fits, for each AD, for 15 energy bins plus the full energy spectrum, are shown in Figures 4, 5, 6, and 7. Each point represents one run. The fact that, for most points, the effective reactor power is above 0.5 (and in fact, for EH1, cluster around 0.5 and near 1.0) simply reflects the fluctuations shown in Fig. 3. The last plot, integrating over the full energy spectrum and included here only for illustration, does not include a correction for disappearance probability.

For plots in energy bins where the IBD rate is large (See Fig. 2) the slope is clearly evident, but at high energies the slope is less apparent. We do not plot error bars on the points, because at high energies, the statistics are very sparse, and using the Poisson-based “ $\sqrt{n}$ ” prescription is misleading.

Before converting the slopes to yield, it is worthwhile to consider the constant term  $\mathcal{R}_0(E_{\text{lo}}, E_{\text{hi}})$  in Eq. 7 and compare it to the background estimates determined by the collaboration. Figure 8 plots  $\mathcal{R}_0(E_{\text{lo}}, E_{\text{hi}})$  as a function of  $E = (E_{\text{lo}} + E_{\text{hi}})/2$ . The results are clearly consistent.

## 6 Yield Results

Our job now is to extract the yield  $Y(E)$  from the slope  $K\epsilon(E)Y(E)$  derived from the linear fits to Eq. 7 shown in Figures 4, 5, 6, and 7. To do this we need the detector efficiency  $\epsilon(E)$  and the average thermal energy per fission  $\bar{e}$ . Note that [25] tabulates all the values  $L_i$  needed to calculate  $K$ .

The detector efficiency includes the effects of all the selection cuts and fundamental detector inefficiencies, for example the neutron capture and Gd- $\gamma$  detection probabilities. The efficiency  $\epsilon(E)$  rises abruptly from zero at 0.3 MeV [24], due to the trigger behavior,

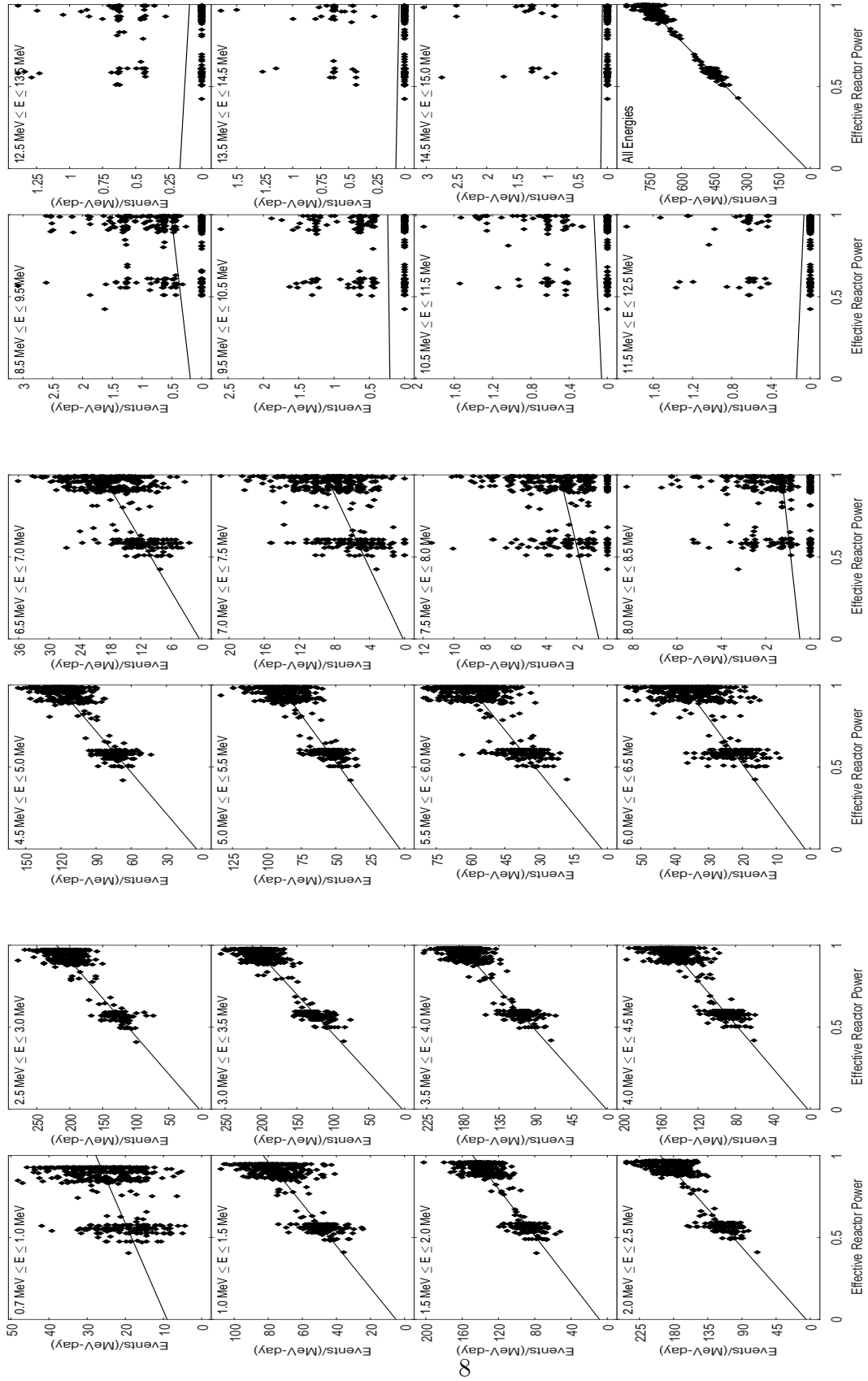


Figure 4: Fit of rate versus effective reactor power for EH1 AD1



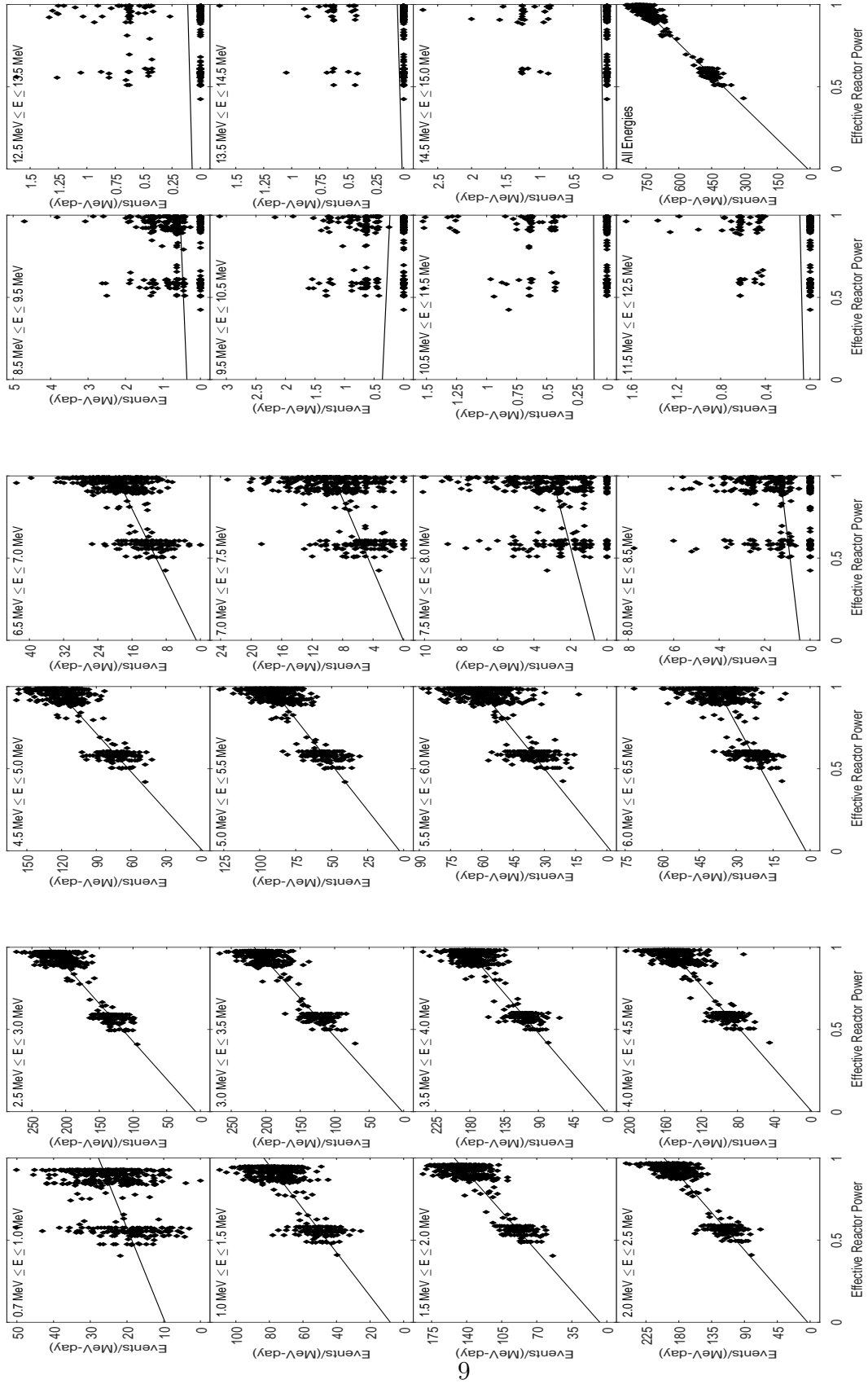


Figure 5: Fit of rate versus effective reactor power for EH1 AD2

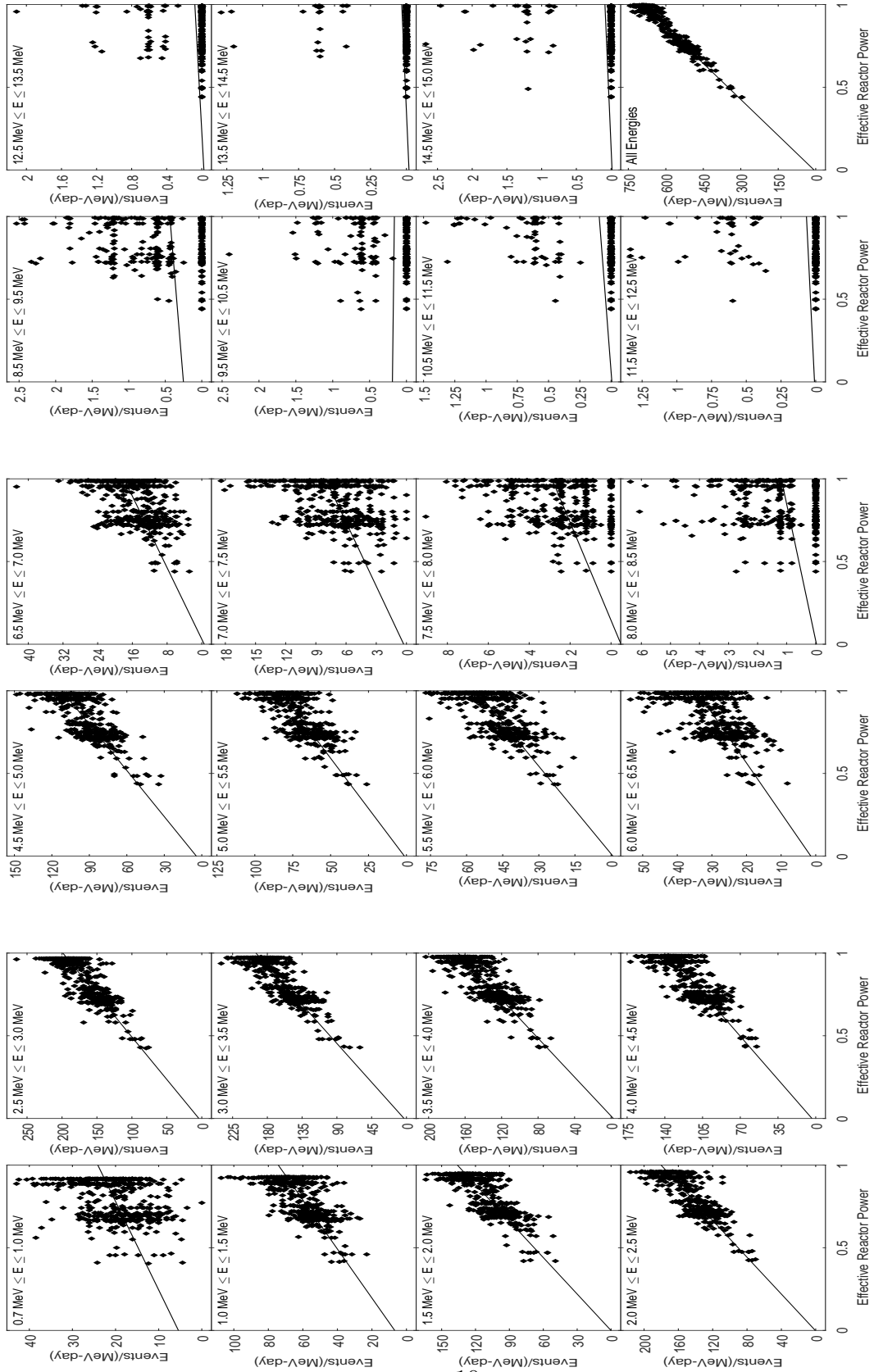


Figure 6: Fit of rate versus effective reactor power for EH2 AD1

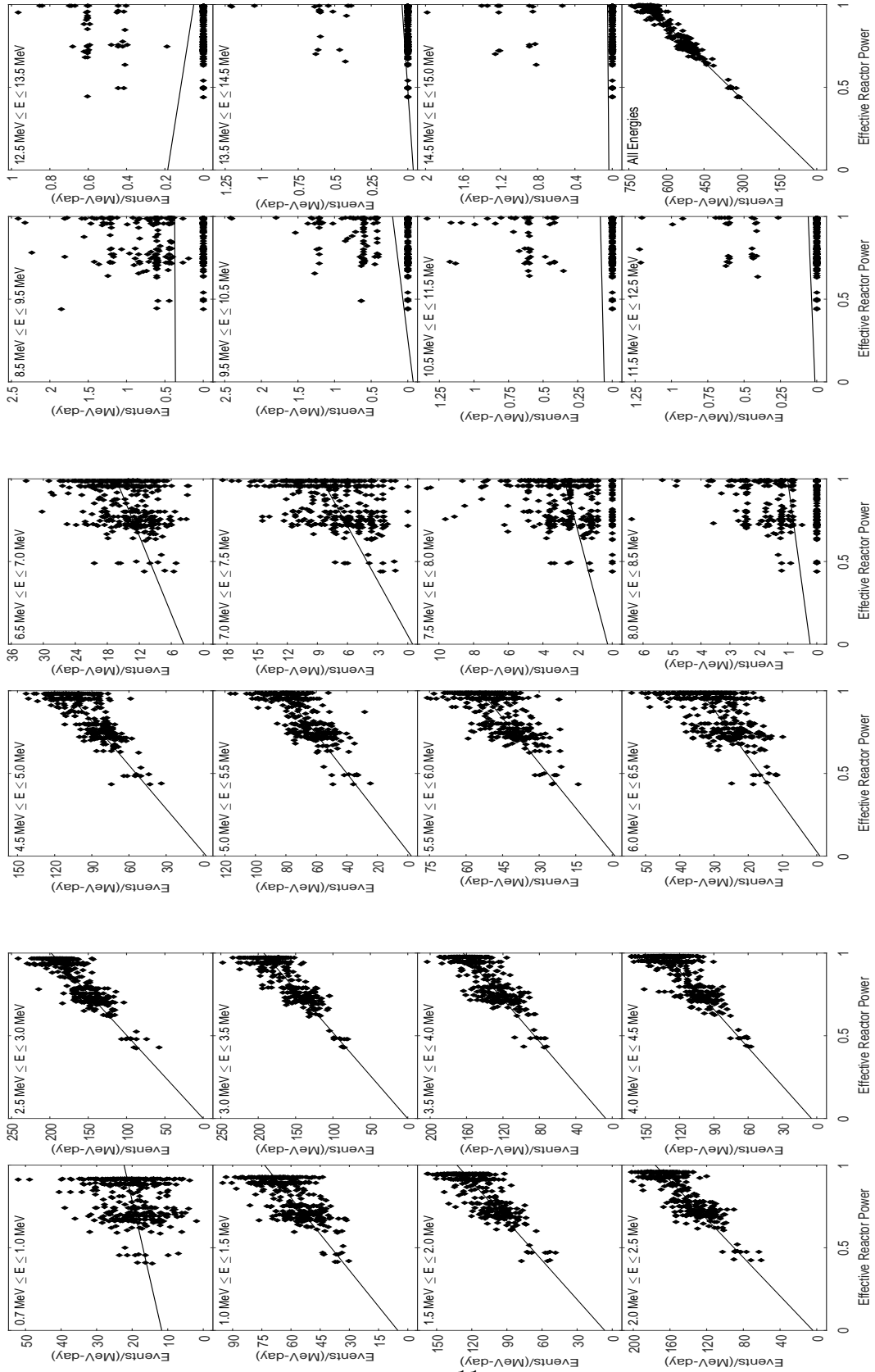


Figure 7: Fit of rate versus effective reactor power for EH2 AD2

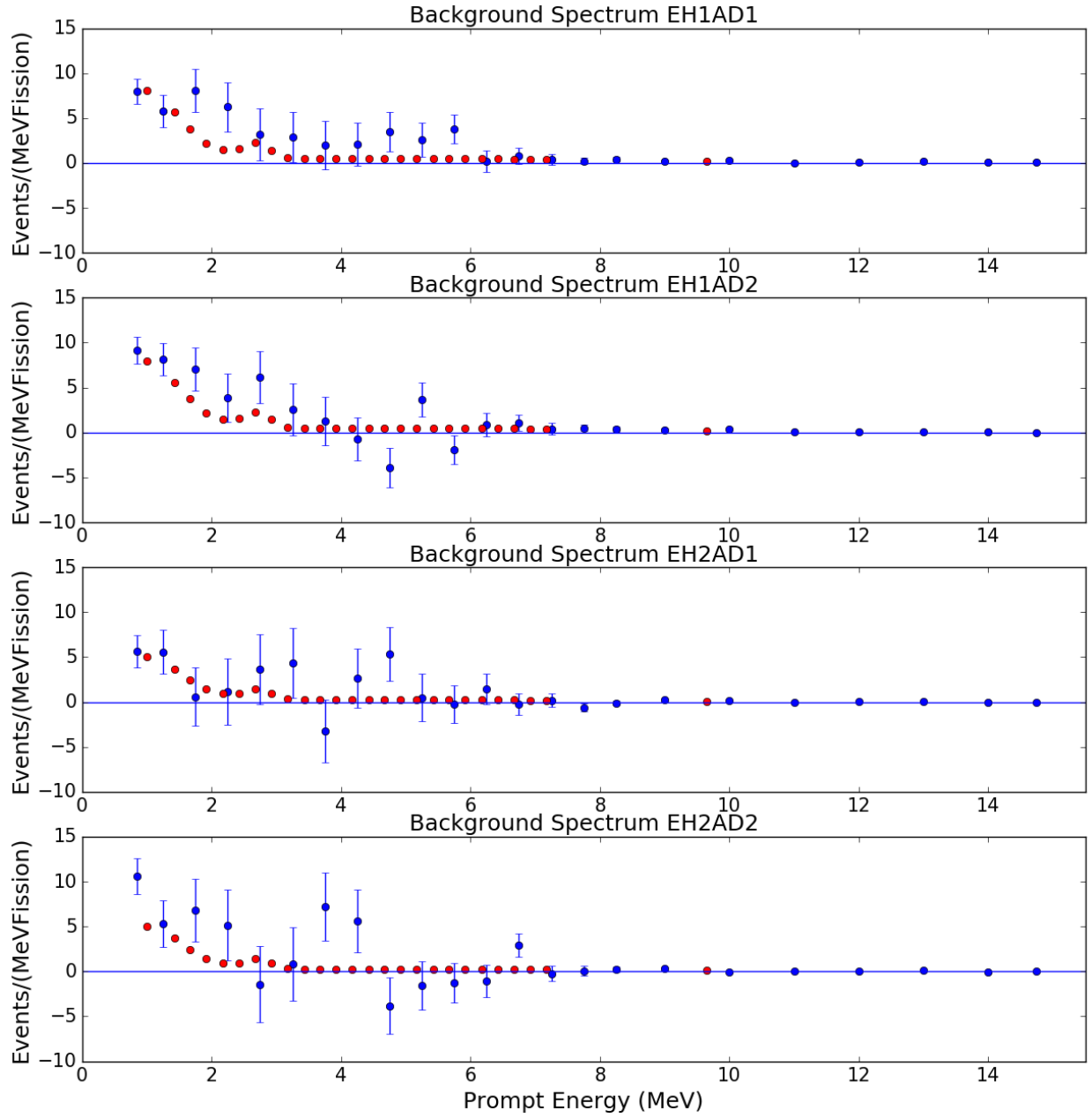


Figure 8: Background rates in the four near detectors as a function of energy. The points with error bars are the fitted values from Eq. 7, that is  $\mathcal{R}_0(E)$ . The red points are the cumulative background estimates as determined by the collaboration and described in [5].

Table 2: Fuel component fractions and energy per fission used in this analysis.

Quantity	$^{235}\text{U}$	$^{238}\text{U}$	$^{239}\text{Pu}$	$^{241}\text{Pu}$
Fuel fraction $f_k$	0.586	0.076	0.288	0.050
MeV/fission $e_k$	202.36	205.99	211.12	214.26

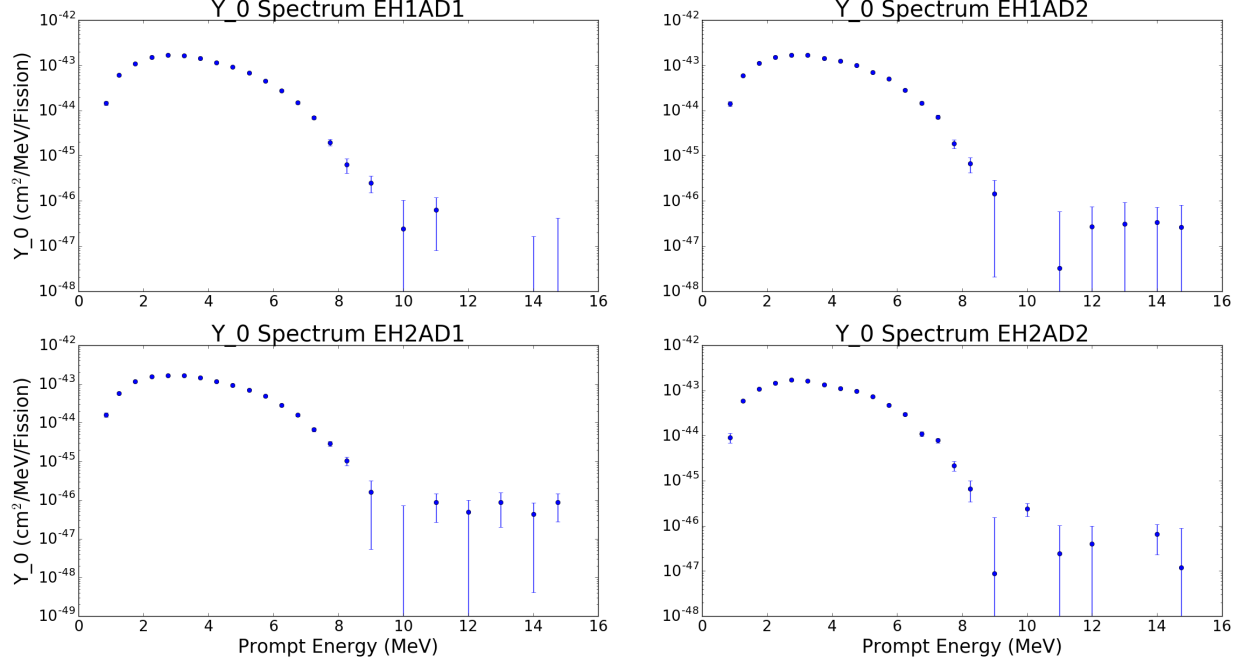


Figure 9: Plot of the extracted yields for all four near-hall antineutrino detectors. The log scale makes it possible to see the behavior at high energies. There is good evidence of a nonzero antineutrino flux above  $E = 8$  MeV.

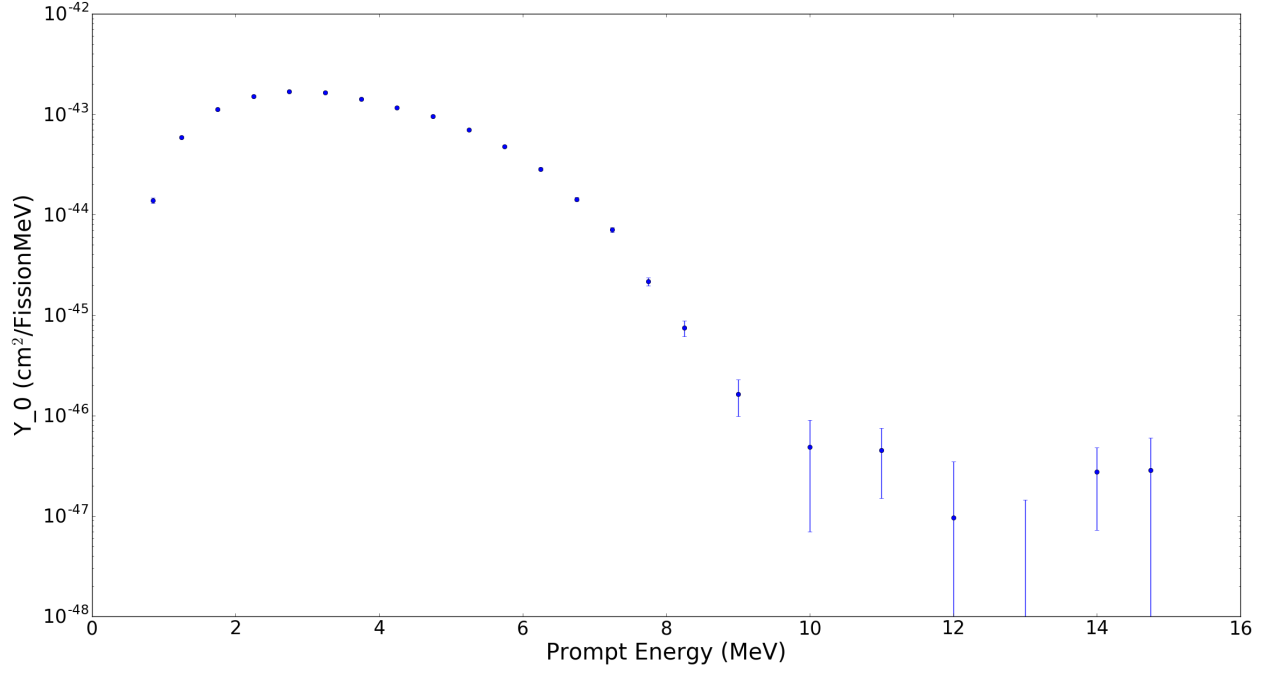
to a nearly constant value of  $80.6 \pm 2.1\%$  [5, 20] at 0.4 MeV. This analysis, then, takes a constant efficiency of  $\epsilon = 0.806$ , independent of energy.

Now consider the calculation of  $\bar{e}$ . As the isotopes  $^{235}\text{U}$ ,  $^{238}\text{U}$ ,  $^{239}\text{Pu}$ , and  $^{241}\text{Pu}$  account for 99.9% of the thermal power [19], we only consider these fuel components. Averaging over these components, we calculate  $\bar{e} = \sum_k f_k e_k$  using the values for  $f_k$  [20] and  $e_k$  [19] listed in Table 2. The result is  $\bar{e} = 205.75$  MeV/fission.

Figure 9 plots the extracted yields, in units of  $\text{cm}^2/\text{fission}$ , individually for all four ADs. The integrated yield  $\int Y(E)dE$ , in  $10^{-45} \text{ cm}^2/\text{fission}$ , for each AD is

EH1 AD1	586.26	$\pm$	6.78	EH2 AD1	588.89	$\pm$	6.99
EH1 AD2	601.35	$\pm$	6.94	EH2 AD2	575.47	$\pm$	6.90

Figure 10 plots and tabulates the bin-by-bin average yield. The final table entry sums over all energy bins, and can be used to compare to the result from [20]. We find  $\int Y(E)dE =$



$E$	$Y$ ( $10^{-45}$ cm <sup>2</sup> /fiss)			$E$	$Y$ ( $10^{-45}$ cm <sup>2</sup> /fiss)		
0.7-1.0	13.85	$\pm$	0.88	6.5-7.0	14.27	$\pm$	0.69
1.0-1.5	59.25	$\pm$	1.36	7.0-7.5	7.072	$\pm$	0.354
1.5-2.0	111.52	$\pm$	2.05	7.5-8.0	2.165	$\pm$	0.203
2.0-2.5	151.18	$\pm$	2.56	8.0-8.5	0.745	$\pm$	0.129
2.5-3.0	168.67	$\pm$	2.78	8.5-9.5	0.164	$\pm$	0.065
3.0-3.5	165.01	$\pm$	2.72	9.5-10.5	0.0484	$\pm$	0.0415
3.5-4.0	141.84	$\pm$	2.41	10.5-11.5	0.0449	$\pm$	0.0299
4.0-4.5	116.78	$\pm$	2.07	11.5-12.5	0.0096	$\pm$	0.0252
4.5-5.0	95.58	$\pm$	1.78	12.5-13.5	-0.0168	$\pm$	0.0313
5.0-5.5	70.14	$\pm$	1.45	13.5-14.5	0.0276	$\pm$	0.0204
5.5-6.0	47.64	$\pm$	1.11	14.5-15.0	0.0287	$\pm$	0.0310
6.0-6.5	28.49	$\pm$	0.81	<b>Integrated</b>	587.93	$\pm$	3.45

Figure 10: Antineutrino yield as a function of prompt energy, averaged over all four ADs. There would seem to be a statistically significant excess up to 10 MeV and possibly higher.

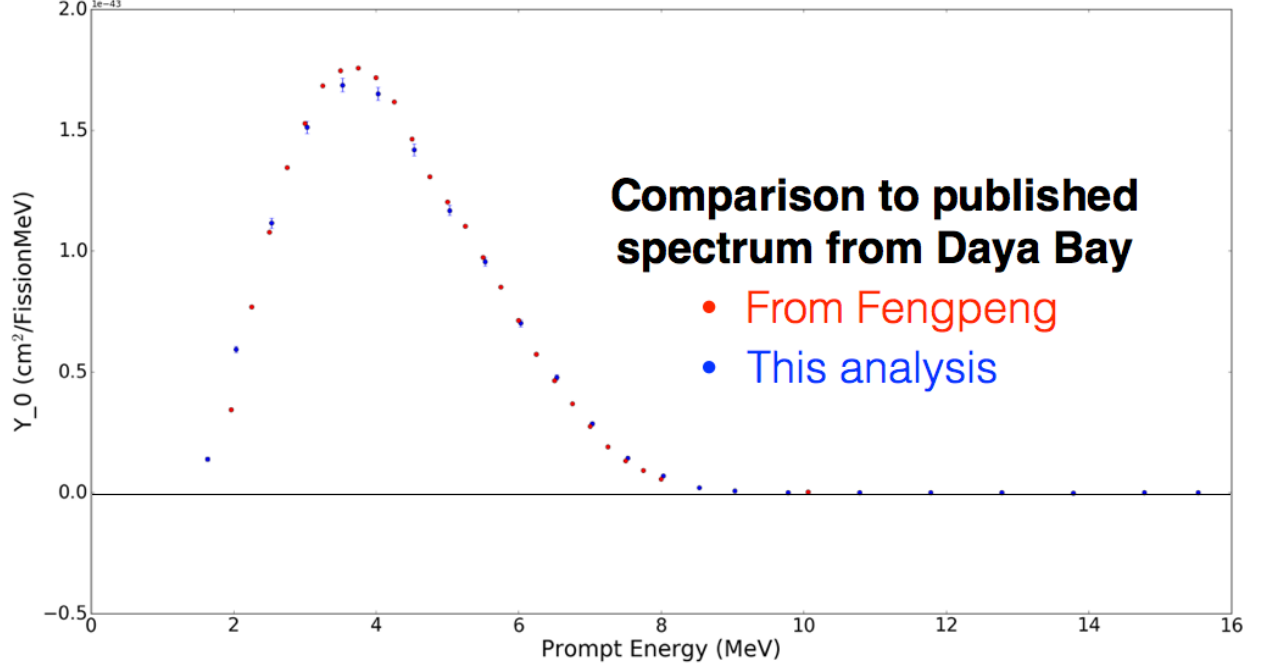


Figure 11: This analysis spectrum, in different energy bins than compiled above, compared to the published [20] spectrum.

$(587.93 \pm 3.45) \times 10^{-45} \text{ cm}^2/\text{fission}$ , where the error is statistical only. The collaboration has published [20]  $\int Y(E)dE = (592 \pm 14) \times 10^{-45} \text{ cm}^2/\text{fission}$ .

As a final check, Figure 11 compares the published [20] Daya Bay spectrum with this analysis, rebinned in energy to match the publication. The disagreement at low energies is an artifact of the need to unfold the energy resolution, which we have not attempted here.

## 7 Comparison to Spectrum Predictions

In order to test our results against different spectrum models  $S(E_\nu)$ , we multiply them by the neutrino cross section  $\sigma_{\text{IBD}}(E_\nu)$  and plot this against our result for  $Y(E) = \sigma_{\text{IBD}}(E_\nu)S(E_\nu)$ . We use the lowest order [29] result, namely

$$\sigma_{\text{IBD}}(E_\nu) = 0.0952 \left[ \frac{E_e p_e}{1 \text{ MeV}^2} \right] \times 10^{-42} \text{ cm}^2 \quad (10)$$

where  $E_e$  is the positron total (i.e kinetic plus  $mc^2$ ) energy and  $p_e$  is the positron momentum.

Our focus here is on the high energy portion of the spectrum. Up until a few years ago, most predictions for  $S(E_\nu)$  came from inverting [14, 15] the fission electron spectra measured by groups at ILL [30, 31, 32]. However, the ILL measurements only extended to electron energies of  $\approx 8 \text{ MeV}$ , so the results are not particularly applicable to this study.

Instead, we will make comparisons to so-called *ab initio* [19] calculations, which directly sum over the thousands of fission fragment nuclei and beta decay branches. Not all of these

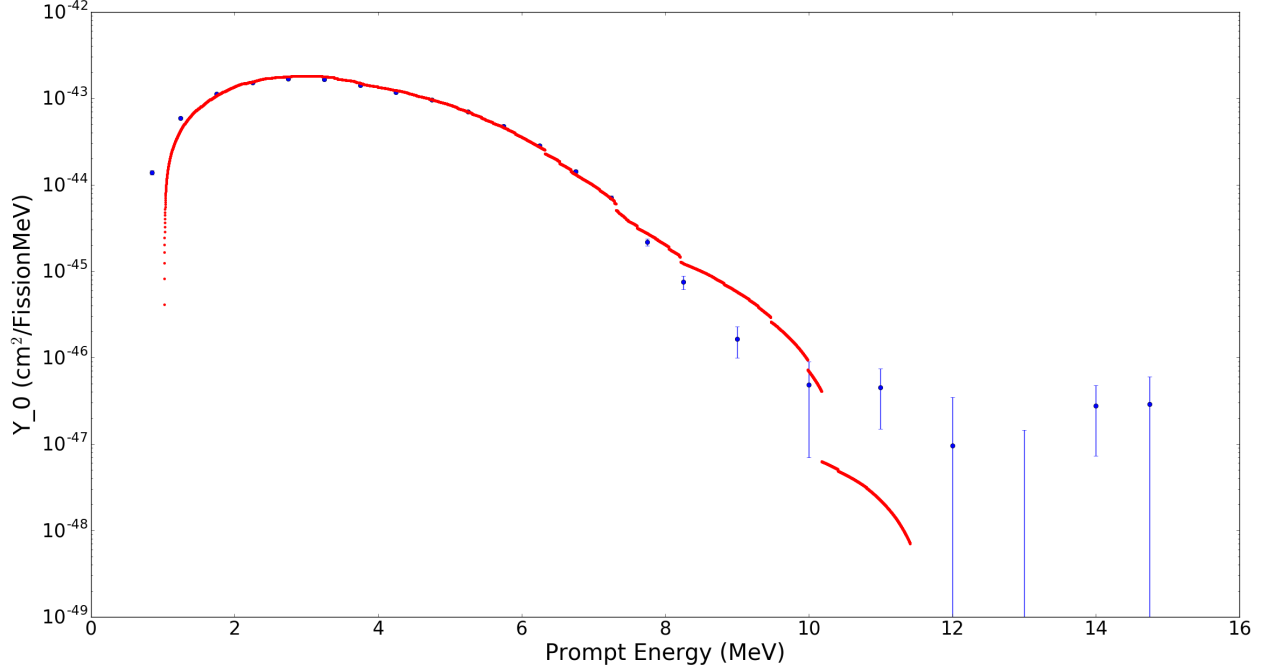


Figure 12: Comparison of our  $Y(E)$  with the calculation by Dwyer and Langford [16].

are well known, and we resort to data base compilations based on evaluations of data, where available, and calculations to fill in the gaps. We confine our comparison to two such data bases, namely ENDF/B-VII.1 and JEFF-3.1, which provide values for the fractional yield of isotopes, and ENSDF for the beta decay branches. These data bases are available online at

ENDF: <http://www.nndc.bnl.gov/exfor/endl00.jsp>

JEFF: <http://www.oecd-neo.org/dbdata/jeff/>

ENSDF: <http://www.nndc.bnl.gov/ensdf/>

It is not uncommon for ENDF and JEFF to have large disagreements for some isotopes. In fact, a recent evaluation of  $^{235}\text{U}$  thermal neutron fission fragment data [33] indicates larger variations in the predicted spectrum at energies above  $\approx 7$  MeV.

Figure 12 shows a comparison of our analysis with the spectrum derived by one such *ab initio* calculation [16], which was actually focussed on the spectrum structure near 5 MeV. The disagreement at high energy is not surprising, since many of those isotopes have less robust data in the ENDF and ENSDF data bases and were not included.

In order to focus on the highest energies, we extract from the databases isotope data for the highest  $Q_\beta$  isotopes with reasonably high cumulative fission probabilities, summing over the four fuel elements. Table 3 lists the known isotopes that should contribute to the neutrino spectrum above 10 MeV. The isotope (or isomer) is listed along with its spin and parity  $J^\pi$ ; the mass difference  $Q^-$  with the daughter nucleus; the beta endpoint energy  $Q_\beta^{\max}$



Table 3: Isotopes with cumulative fission yield  $\geq 10^{-6}$  and  $Q \geq 10$  MeV.

Isotope	$J^\pi$	$Q^-$ (keV)	$Q_\beta^{\max}$ (MeV)	Fission Yield	
				ENDF	JEFF
$^{84}\text{Ga}$	$(0^-)$	13690	13.69	$6.53 \times 10^{-5}$	$3.17 \times 10^{-5}$
$^{84}\text{Ga}^*$	$(3^-, 4^-)$	13690	13.07	$6.53 \times 10^{-5}$	$3.17 \times 10^{-5}$
$^{100}\text{Rb}$	$(3^+, 4^-)$	13128	13.00	$2.04 \times 10^{-4}$	$6.08 \times 10^{-7}$
$^{98}\text{Rb}$	$(0, 1)$	12326	12.18	$9.17 \times 10^{-5}$	$3.169 \times 10^{-5}$
$^{98}\text{Rb}^*$	$(3, 4)$	12596	12.12	$9.17 \times 10^{-5}$	$3.169 \times 10^{-5}$
$^{92}\text{Br}$	$(?)$	12537	12.54	$3.49 \times 10^{-4}$	$2.7 \times 10^{-4}$
$^{114}\text{Tc}$	$(\geq 4)$	11785	11.79	$1.89 \times 10^{-6}$	$1.07 \times 10^{-6}$
$^{96}\text{Rb}$	$2^+$	11571	10.76	$2.3 \times 10^{-3}$	$1.29 \times 10^{-3}$
$^{80}\text{Ga}$	$(3)$	10380	10.38	$9.34 \times 10^{-5}$	$1.37 \times 10^{-4}$
$^{84}\text{As}$	$(3^-)$	10094	10.09	$1.07 \times 10^{-3}$	$9.68 \times 10^{-4}$
$^{90}\text{Br}$	$(?)$	10350	10.35	$5.0 \times 10^{-3}$	$4.1 \times 10^{-3}$
$^{108}\text{Nb}$	$(2^+)$	10607	10.41	$2.056 \times 10^{-5}$	$6.68 \times 10^{-5}$
$^{93}\text{Br}$	$(5/2^-)$	11090	11.09	$7.79 \times 10^{-5}$	$4.466 \times 10^{-5}$
$^{97}\text{Rb}$	$3/2^+$	10432	10.43	$3.27 \times 10^{-4}$	$4.4 \times 10^{-4}$
$^{130}\text{In}$	$1^-$	10249	10.25	$7.3 \times 10^{-4}$	$3.2 \times 10^{-4}$

of the most energetic known decay; and the cumulative fission yield. The spin, parity, and  $Q$ -values are from ENSDF, and the fissions yields according to ENDF or JEFF are listed separately. If the spin and/or parity of the isotope is not well established, it is in parentheses, in some cases with the most likely values. In some cases, the spin and/or parity is unknown.

Table 3 only lists isotopes with fission yield greater than  $10^{-6}$ . In most cases, the fission yields from ENDF and JEFF are close to each other, but  $^{100}\text{Rb}$  is a notable exception.

To get a predicted beta spectrum at high energy, we sum over these isotopes, adding up their individual beta spectra and multiplying by the IBD cross section, Eq. 10. All spectrum shapes are assumed to be allowed, since we do not know well the initial or final state spins and parities, but it is highly likely that the transitions are forbidden, at varying degrees. The Fermi Coulomb factor is included [19]; it is worth noting that in Fermi's original paper [34] the so-called Coulomb factor is a correction for the density of states, so it applies to neutrino emission as well as  $\beta^\mp$  emission.

The result is shown in Figures 13 and 14. There is generally better agreement with the values from ENDF, but with the marginal statistics and the potential for significant shape changes for forbidden transitions, it is difficult to draw too many conclusions. Probably most significant is the possible nonzero flux above 14 MeV; it would appear there are no known isotopes that would account for this flux.

How strong is the evidence for very high energy neutrinos? The average of the five prompt energy bins with  $E > 11$  MeV gives an average yield  $(0.020 \pm 0.012) \times 10^{-45}$  cm<sup>2</sup>/fission. This is enticing, but clearly more data is needed to make any firm conclusion.

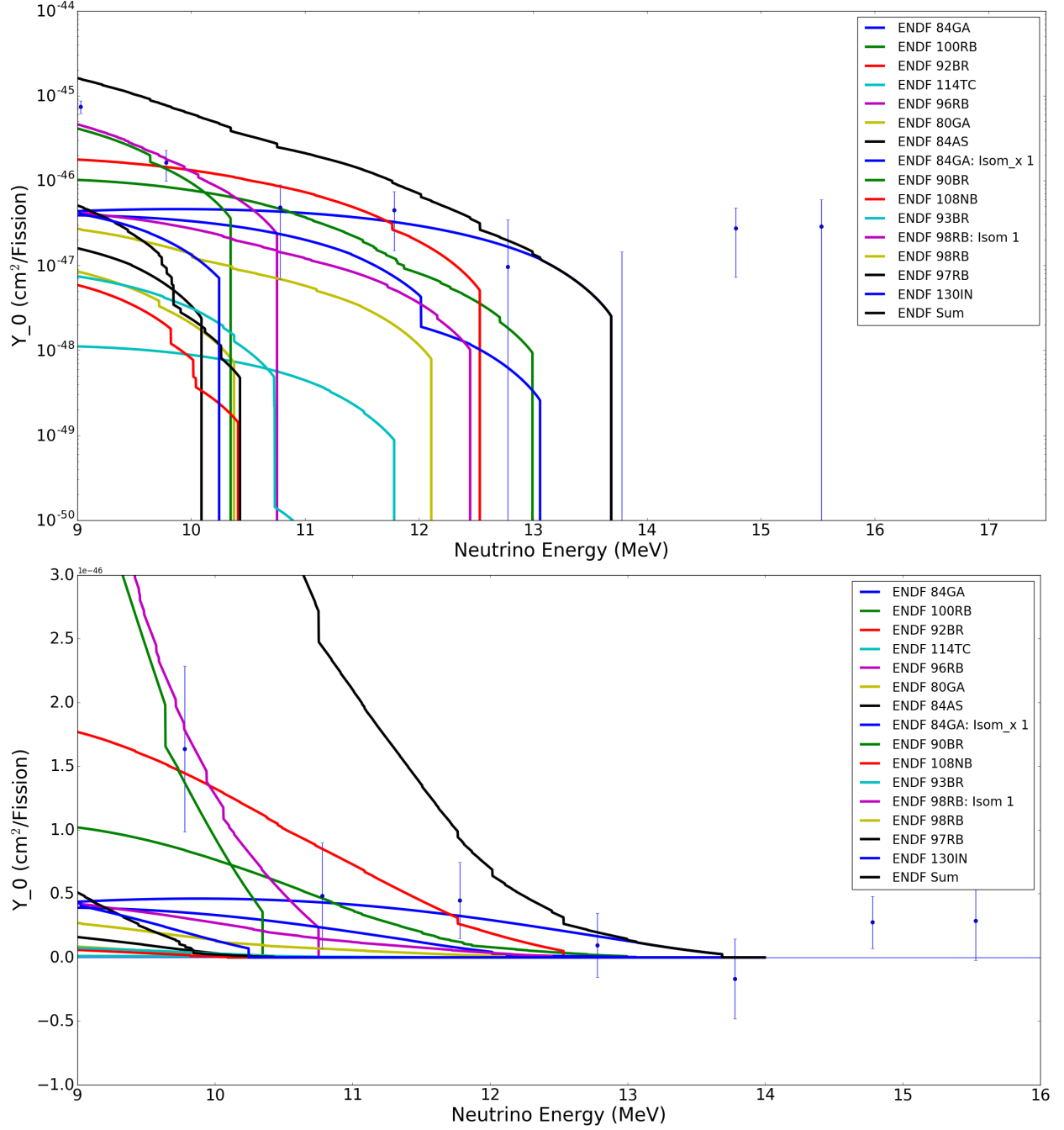


Figure 13: Comparison of our  $Y(E)$  at high energy with the isotopes shown in Table 3, using values from the **ENDF** data base.

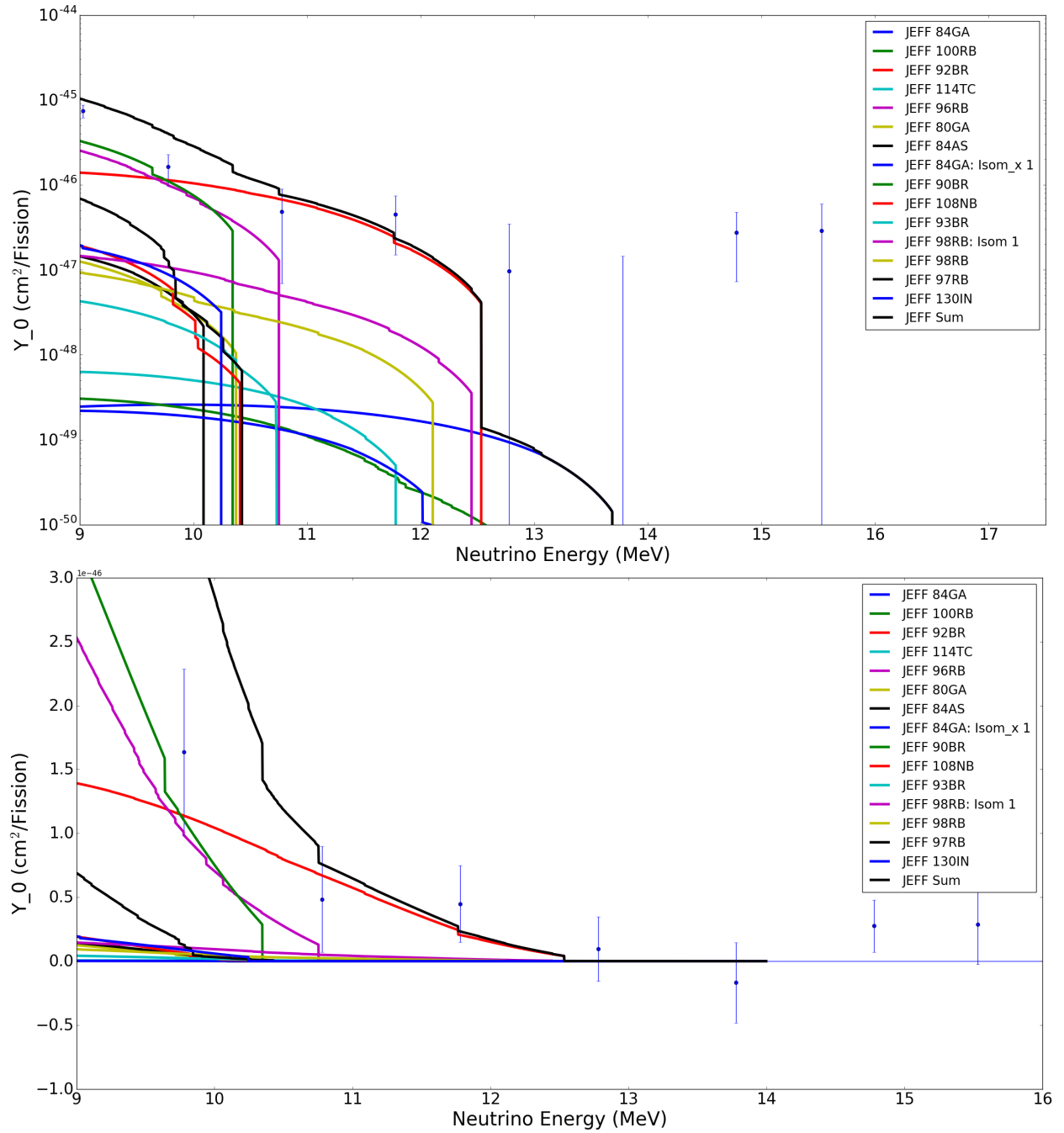


Figure 14: Comparison of our  $Y(E)$  at high energy with the isotopes shown in Table 3, using values from the **JEFF** data base.

## 8 Conclusion

An analysis procedure has been developed which appears to be sound, using correlations between IBD rate and reactor power fluctuations to determine the reactor neutrino yield. Only statistical errors are considered so far, but there is agreement both with methods which integrate over long periods of reactor operation, as well as with the collaborations' estimates of background as a function of energy.

There is clearly a nonzero flux for prompt energies above 8 MeV, possibly past 10 MeV, but higher statistics are necessary to establish this. It does seem, however, that the tail of the “Reactor  $\bar{\nu}_e$ ” in Fig. 1 does not fall as rapidly as previously suggested. This is of particular interest to those designing experiments to search for the diffuse supernova neutrino background.

Further work falls into two categories:

### 1. Increasing statistics with more data.

- Apply this analysis to larger data sets when they become available. (Perhaps  $\times 2$  increase in statistics?)
- Select data for  $np$  capture events above some reasonable prompt energy threshold. (Perhaps another  $\times 2$  increase in statistics?)
- Extend this analysis to the four ADs in EH3. (Smaller statistical increase, but lower background, so it is at least a cross check.)

### 2. Continued analysis of high energy spectrum shape.

- Come up with better estimates for the increases “ $\times 2$ ” and “ $\times 2$ ” expected from new data sets and  $np$  capture analysis.
- Study effects of differences between AdSimple [35, 36] and AdScaled [37, 38] energy reconstruction, especially for events with large prompt energy signals.
- Include a study of systematic uncertainties, at least to rule out their significant contribution at high energies, but also to establish agreement with the published spectrum at low energies.
- Demonstrate the importance of the Fermi function (aka the Coulomb correction) for high energy neutrinos, that is, low energy beta electrons, for the decays in Table 3.
- Demonstrate the importance of forbidden corrections to the beta decays in Table 3, within the best guesses for spins and parities of initial and final states.
- Test adjustment of isotope components to make better fits to data. There is some tradeoff to working in the region  $8 \leq E \leq 10$  MeV as opposed to higher energies where there are fewer components, but this will likely require higher statistics than we have already acquired.)

## References

- [1] K. Eguchi et al. First results from KamLAND: Evidence for reactor anti-neutrino disappearance. *Phys. Rev. Lett.*, 90:021802, 2003.
- [2] T. Araki et al. Measurement of neutrino oscillation with KamLAND: Evidence of spectral distortion. *Phys. Rev. Lett.*, 94:081801, 2005.
- [3] S. Abe et al. Precision Measurement of Neutrino Oscillation Parameters with KamLAND. *Phys. Rev. Lett.*, 100:221803, 2008.
- [4] F. P. An et al. Observation of electron-antineutrino disappearance at Daya Bay. *Phys. Rev. Lett.*, 108:171803, 2012.
- [5] F. P. An et al. Improved Measurement of Electron Antineutrino Disappearance at Daya Bay. *Chin. Phys.*, C37:011001, 2013.
- [6] F. P. An et al. Spectral measurement of electron antineutrino oscillation amplitude and frequency at Daya Bay. *Phys. Rev. Lett.*, 112:061801, 2014.
- [7] F. P. An et al. New Measurement of Antineutrino Oscillation with the Full Detector Configuration at Daya Bay. *Phys. Rev. Lett.*, 115(11):111802, 2015.
- [8] J. K. Ahn et al. Observation of Reactor Electron Antineutrino Disappearance in the RENO Experiment. *Phys. Rev. Lett.*, 108:191802, 2012.
- [9] Y. Abe et al. Reactor electron antineutrino disappearance in the Double Chooz experiment. *Phys. Rev.*, D86:052008, 2012.
- [10] Y. Abe et al. Background-independent measurement of  $\theta_{13}$  in Double Chooz. *Phys. Lett.*, B735:51–56, 2014.
- [11] Y. Abe et al. Improved measurements of the neutrino mixing angle  $\theta_{13}$  with the Double Chooz detector. *JHEP*, 10:086, 2014. [Erratum: JHEP02,074(2015)].
- [12] B. R. Davis, P. Vogel, F. M. Mann, and R. E. Schenter. Reactor Anti-neutrino Spectra and Their Application to Anti-neutrino Induced Reactions. *Phys. Rev.*, C19:2259–2266, 1979.
- [13] P. Vogel, G. K. Schenter, F. M. Mann, and R. E. Schenter. Reactor Anti-neutrino Spectra and Their Application to Anti-neutrino Induced Reactions. 2. *Phys. Rev.*, C24:1543–1553, 1981.
- [14] Th. A. Mueller et al. Improved Predictions of Reactor Antineutrino Spectra. *Phys. Rev.*, C83:054615, 2011.
- [15] Patrick Huber. On the determination of anti-neutrino spectra from nuclear reactors. *Phys. Rev.*, C84:024617, 2011. [Erratum: Phys. Rev.C85,029901(2012)].

- [16] D. A. Dwyer and T. J. Langford. Spectral Structure of Electron Antineutrinos from Nuclear Reactors. *Phys. Rev. Lett.*, 114(1):012502, 2015.
- [17] A. A. Sonzogni, T. D. Johnson, and E. A. McCutchan. Nuclear structure insights into reactor antineutrino spectra. *Phys. Rev.*, C91(1):011301, 2015.
- [18] A. C. Hayes, J. L. Friar, G. T. Garvey, Gerard Jungman, and Guy Jonkmans. Systematic Uncertainties in the Analysis of the Reactor Neutrino Anomaly. *Phys. Rev. Lett.*, 112:202501, 2014.
- [19] A. C. Hayes and P. Vogel. Reactor Neutrino Spectra. *Ann. Rev. Nucl. Part. Sci.*, 66(1):1, 2016.
- [20] Feng Peng An et al. Measurement of the Reactor Antineutrino Flux and Spectrum at Daya Bay. *Phys. Rev. Lett.*, 116(6):061801, 2016.
- [21] A. C. Hayes, J. L. Friar, G. T. Garvey, Duligur Ibeling, Gerard Jungman, T. Kawano, and Robert W. Mills. Possible origins and implications of the shoulder in reactor neutrino spectra. *Phys. Rev.*, D92(3):033015, 2015.
- [22] John F. Beacom. The Diffuse Supernova Neutrino Background. *Ann. Rev. Nucl. Part. Sci.*, 60:439–462, 2010.
- [23] John F. Beacom and Mark R. Vagins. GADZOOKS! Anti-neutrino spectroscopy with large water Cherenkov detectors. *Phys. Rev. Lett.*, 93:171101, 2004.
- [24] F. P. An et al. A side-by-side comparison of Daya Bay antineutrino detectors. *Nucl. Instrum. Meth.*, A685:78–97, 2012.
- [25] F. P. An et al. The Detector System of The Daya Bay Reactor Neutrino Experiment. *Nucl. Instrum. Meth.*, A811:133–161, 2016.
- [26] Neill Raper. *High Energy Reactor Neutrinos*. PhD thesis, Rensselaer Polytechnic Institute, April 2016.
- [27] Matt Kramer. AdSimple vs. AdScaled: Nonuniformity and  $n$ Gd efficiency in P15A. Report DocDB-11053-v2, UC Berkeley, 2016.
- [28] K. A. Olive et al. Review of Particle Physics. *Chin. Phys.*, C38:090001, 2014.
- [29] P. Vogel and John F. Beacom. Angular distribution of neutron inverse beta decay,  $\bar{\nu}_e + p \rightarrow e^+ + n$ . *Phys. Rev.*, D60:053003, 1999.
- [30] K. Schreckenbach, G. Colvin, W. Gelletly, and F. Von Feilitzsch. DETERMINATION OF THE ANTI-NEUTRINO SPECTRUM FROM U-235 THERMAL NEUTRON FISSION PRODUCTS UP TO 9.5-MEV. *Phys. Lett.*, B160:325–330, 1985.

- [31] F. Von Feilitzsch, A. A. Hahn, and K. Schreckenbach. EXPERIMENTAL BETA SPECTRA FROM PU-239 AND U-235 THERMAL NEUTRON FISSION PRODUCTS AND THEIR CORRELATED ANTI-NEUTRINOS SPECTRA. *Phys. Lett.*, B118:162–166, 1982.
- [32] A. A. Hahn, K. Schreckenbach, G. Colvin, B. Krusche, W. Gelletly, and F. Von Feilitzsch. Anti-neutrino Spectra From  $^{241}\text{Pu}$  and  $^{239}\text{Pu}$  Thermal Neutron Fission Products. *Phys. Lett.*, B218:365–368, 1989.
- [33] A.A. Sonzogni, E.A. McCutchan, T.D. Johnson, and P. Dimitriou. Effects of Fission Yield Data in the Calculation of Antineutrino Spectra for  $^{235}\text{U}(n, \text{fission})$  at Thermal and Fast Neutron Energies. *Phys. Rev. Lett.*, 116(13):132502, 2016.
- [34] Fred L. Wilson. Fermi’s Theory of Beta Decay. *Amer. Journal of Physics*, 36:1150, 1968.
- [35] Cheng-Ju Lin, Yasuhiro Nakajima, J. Pedro Ochoa, and Patrick K.V. Tsang. The AdSimple Reconstruction. Report DocDB-7334-v2, UC Berkeley, 2013.
- [36] Matt Kramer and Yury Malyshev. Changes in AdSimple for the P15A production. Report DocDB-10542-v2, UC Berkeley, 2015.
- [37] Zhimin Wang, Liangjian Wen, Zeyuan Yu, and Liang Zhan. Anti-neutrino Detector Energy Response. Report DocDB-7314-v2, IHEP, Beijing, 2011.
- [38] Yu Xu, Masheng Yang, and Zeyuan Yu. AdScaled energy scale constant update for P15A. Report DocDB-7314-v2, IHEP, Beijing, 2011.